

# Probing the precipitation life cycle by iterative rain cell tracking

Christopher Moseley,<sup>1,2</sup> Peter Berg,<sup>3</sup> and Jan O. Haerter<sup>4</sup>

Received 11 September 2013; revised 7 November 2013; accepted 29 November 2013; published 16 December 2013.

[1] Monitoring the life cycle of convective rain cells requires a Lagrangian viewpoint where the observer moves with the dominant background flow. To adopt such a moving reference frame, we design, validate, and apply a simple rain cell tracking method—which we term *iterative rain cell tracking* (IRT)—for spatio-temporal precipitation data. IRT iteratively identifies the formation and dissipation of rain cells and determines the large-scale flow. The iteration is repeated until reaching convergence. As validated using reanalysis wind speeds, repeated iterations lead to substantially increased agreement of the background flow field and an increased number of complete tracks. Our method is thereby able to monitor the growth and intensity profiles of rain cells and is applied to a high-resolution (5 min and  $1 \times 1 \text{ km}^2$ ) data set of radar-derived rainfall intensities over Germany. We then combine this data set with surface temperature observations and synoptic observations to group tracks according to convective and stratiform conditions. Convective tracks show clear life cycles in intensity, with peaks shifted off-center toward the beginning of the track, whereas stratiform tracks have comparatively featureless intensity profiles. Our results show that the convective life cycle can lead to convection-dominating precipitation extremes at short time scales, while track-mean intensities may vary much less between the two types. The observed features become more pronounced as surface temperature increases, and in the case of convection even exceeded the rates expected from the Clausius-Clapeyron relation.

**Citation:** Moseley, C., P. Berg, and J. O. Haerter (2013), Probing the precipitation life cycle by iterative rain cell tracking, *J. Geophys. Res. Atmos.*, 118, 13,361–13,370, doi:10.1002/2013JD020868.

## 1. Introduction

[2] Convection is a process of fundamental interest in climate research due to its influence on the earth's radiation budget and precipitation. Observations [Lenderink and van Meijgaard, 2008] and recent simulations [Singleton and Toumi, 2012] have suggested that convective precipitation intensity may react in a substantially different way to temperature changes than is the case for stratiform precipitation. This hypothesis was recently backed by observational support for a midlatitude region by Berg *et al.* [2013].

[3] Specifically, precipitating convective systems have been characterized in terms of a life cycle where updrafts caused by surface heating lead to lifting and condensation

of moist air, yielding further buoyancy and divergence aloft [Chen *et al.*, 2012]. Convective updrafts are balanced by downdrafts away from the center. After onset of precipitation, evaporative cooling has been suggested to cause downdrafts even in cell centers, counteracting further convective activity, thus completing the life cycle. To monitor convective structures, measurements made by a stationary temporal observer (e.g., a rain gauge) or a spatial observer (e.g., radar and satellite images at isolated times) may lead to little insight into their dynamics, as they travel with the prevailing flow field during their lifetime and only a section of the actual life cycle can be observed. Proper characterization of the dynamics of such systems demands a *Lagrangian* view where the observer travels in the moving reference frame of the cloud. The Lagrangian observer can be regarded as a third alternative to a purely temporal or a purely spatial observer.

[4] Various objective tracking methods have been developed and advanced during the last 2 decades, mainly for the purpose of nowcasting strong convective events like thunderstorms [Rosenfeld, 1987; Dixon and Wiener, 1993; Wilson *et al.*, 1998; Johnson *et al.*, 1998; Handwerker, 2002; Hering *et al.*, 2005; Novo *et al.*, 2013] but also the mean life cycles of the cell size and statistics of tracked rain cells have been studied [Kysnarova and Novak, 2009; Peleg and Morin, 2012; Rigo *et al.*, 2012]. Other tracking methods have been applied not only to radar data but also to other

<sup>1</sup>Max Planck Institute for Meteorology, Hamburg, Germany.

<sup>2</sup>Helmholtz Zentrum Geesthacht, Climate Service Center, Hamburg, Germany.

<sup>3</sup>Hydrology Unit, Swedish Meteorological and Hydrological Institute, Norrköping, Sweden.

<sup>4</sup>Center for Models of Life, Niels Bohr Institute, Copenhagen, Denmark.

Corresponding author: C. Moseley, Max Planck Institute for Meteorology, Bundesstr. 52, DE-20146 Hamburg, Germany. (christopher.moseley@mpimet.mpg.de)

high-resolution observational data sets such as satellite data [Lakshmanan *et al.*, 2009; Feng *et al.*, 2012].

[5] The main obstacle of these methods is to define what a rain cell is and how to segment it. Further, they have to handle merging and splitting and determine the velocity of the cells. The latter is used to improve tracking results by projecting a given cell into the future to accomplish a better match with the succeeding time step. Often the assumption is made that the changes due to the turbulence of the flow field from one time step to another is small compared to the displacement by the mean flow—an approximation originally known as Taylor’s hypothesis [Taylor, 1938]. Most tracking methods estimate the velocity of single individual cells by following their trajectories from the previous time step to the present one and extrapolating their movement to the next time step.

[6] The iterative rain cell tracking (IRT) method follows a novel approach where the background atmospheric flow is calculated from the tracks in an iterative procedure. This simple method represents a coarse graining of the horizontal advection field, where coarse-grained velocities represent the mean background flow. Convergence of the procedure and comparison to reanalysis data serve as a consistency check. The iterative method allows detection of more, especially smaller, tracks.

[7] On a system level, convergence and divergence of moist and dry air due to a given convective cell may affect surrounding cells. In this sense, convective rain cells could be considered as self-organized dynamical entities where any cell by itself may not behave in the same way as when embedded in a system of cells [Koren and Feingold, 2011; Feingold *et al.*, 2010; Bretherton *et al.*, 2005; Chen *et al.*, 2012]. As the coarse graining retains the small-scale dynamics produced by the precipitation system, this method could hence serve as a starting point for studies focusing on the relative dynamics—i.e., interaction—of neighboring rain cells.

[8] *Convective* precipitation events are traditionally distinguished from *stratiform* events. Some classification methods utilize the detection of a stratiform “bright band” in radar reflectivity [Steiner *et al.*, 1995; Smyth and Illingworth, 1998; Houze Jr., 1997], observed intensity distributions [Llasat, 2001], or cluster analysis [Peleg and Morin, 2012], allowing the identification of even more than two classes. For our study, we use a methodology based on human synoptic cloud observations, previously employed to distinguish the two precipitation types [Berg *et al.*, 2013]. The IRT-derived rain cell tracks are then grouped according to the two categories and characteristics of the two types are extracted.

[9] The aim of the present paper is the study of the response of the convective life cycle to near-surface temperatures, using the IRT method in combination with the convective/stratiform separation as a tool. We describe the IRT method of tracking cells, apply it to a high-resolution radar data set over Germany, and validate the derived large-scale flow with reanalysis data. Life cycle statistics are derived for both convective and stratiform precipitation tracks. The data sets used, and the IRT method are introduced in section 2. Section 3 presents the results for the derivation of flow velocities and sensitivity tests, and section 4 presents the analysis of the track life cycles. The paper closes with discussion and conclusions in section 5.

## 2. Data and Methods

[10] This study uses the RY radar data product provided by the German Weather Service [Crewell *et al.*, 2008]. This is a 1 km × 1 km grid composite of 17 radar stations covering Germany for the 2 year time period 2007–2008. Note that with the relatively stable climate of Germany and the large number of rain cells within a year (on the order of 10<sup>6</sup>; see section 4.1), results from this study are not likely to be sensitive to the particular years studied. Rainfall rates were obtained from raindrop reflectivities using the Z-R relationship [Steiner *et al.*, 2004]. The data set contains discrete instantaneous precipitation intensities every 5 min. Areas outside of the radar coverage change over time depending on the number of active radar devices and data losses and are marked with a code for missing values. The spatial extent of the data set is 900 km × 900 km.

[11] The separation of convective and stratiform precipitation types is performed by using 3-hourly synoptic cloud observations over Germany [Berg *et al.*, 2013]. To make sure the classifications are as robust as possible in both time and space, we aggregate observations over larger sub-regions of the domain, i.e., quadrants defined by the 10°W and 51°N lines of longitude and latitude, respectively. Sensitivity tests of the classification were reported in Berg *et al.* [2013, including supporting information]. For every 3 h period centered on the time of the synoptic observation, each quadrant is associated with either the class C for predominantly convective, class S for predominantly stratiform cloud conditions, class M for co-existence of the two types at a single location, or class N for cases with dominantly missing values. For sensitivity tests, two criteria *Q1* and *Q2* were used for the synoptic classification: Under *Q1*, a quadrant is classified as C (S) if all stations within the quadrant indicate convective (stratiform) and/or mixed conditions, otherwise the classification is M. In other words, classification C cannot contain any stratiform observations within the quadrant, however, observations of mixed convective and stratiform clouds in single stations are allowed. An additional stricter criterion is applied for *Q2*: there must be more numerous observations of C (S) than observations of mixed character. Thus, for *Q2* less than half of the observations in the quadrant can be mixed conditions. Earlier sensitivity analyses of *Q1* and *Q2* showed that there are cases where some contamination of the other precipitation type occurs, but that this is much reduced with the *Q2* criterion [Berg *et al.*, 2013], however, *Q1* is still useful due to its larger sample size and thus more robust statistics. The daily mean temperature has earlier been shown to be useful for studying the relationship between precipitation intensity and temperature [Lenderink and van Meijgaard, 2008; Berg *et al.*, 2013], and we therefore make use of the daily mean temperature from the E-OBS observational data set [Haylock *et al.*, 2008].

[12] The tracking algorithm is visualized in the flowchart in Figure 1. In the first step (Figure 1a), rain cells are detected for every radar image individually. A cell is defined as a contiguous area of grid points above a lower threshold (see section 3), such that directly neighbored precipitating grid points belong to the same cell. Diagonal neighborhood is excluded. Cells adjacent to the outer boundaries or to missing values are removed (Figure 1b). For each cell, the area, area-integrated intensity, the location of the intensity weighted center of mass, and the daily mean temperature at

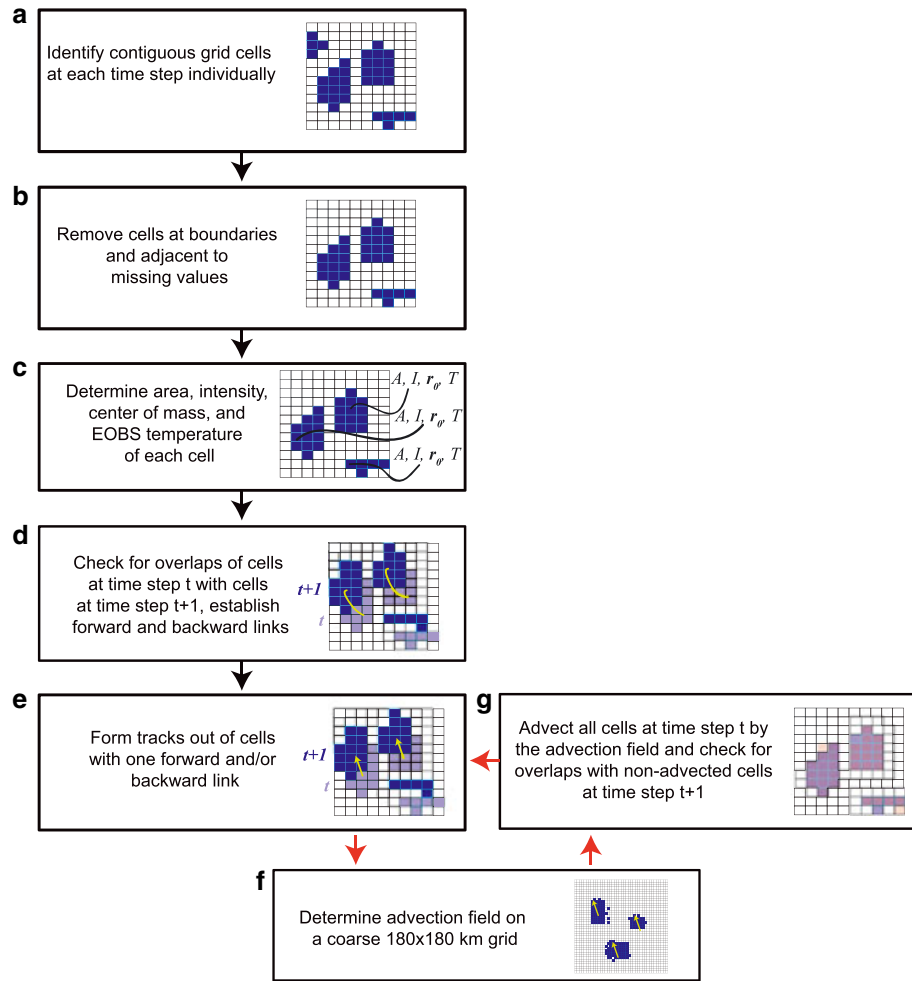


**Figure 1.** Flowchart of iterative tracking procedure. (a–d) Algorithmic steps carried out only once. (e–g) Steps carried out iteratively during the IRT method. Bold black (red) arrows between flow boxes denote sequence of algorithm for single (iterative) procedures. Blue- and purple-shaded regions in schematics are regions of rain. White squares are regions without rain. Yellow arrows (links) in Figures 1e and 1f (Figure 1d) denote translation of rain areas (association of rain areas by overlap).

the center of mass are recorded (Figure 1c). Each cell at a given time step  $t$  is checked for overlaps (at least one pixel) with cells of the consecutive time step  $t + 1$  and the preceding time step  $t - 1$  (Figure 1d). By this procedure, we establish forward and backward links between cells in time: Each cell can have either zero, one, or more than one forward and backward connection. Sometimes it happens that a cell overlaps with missing values or deleted cells from the previous or the subsequent time step. These cases are flagged in order to identify tracks which are corrupted by missing values or boundary effects, so that they can be removed from the statistics after the tracking. In the following step (Figure 1e), tracks are formed: Cells with one and only one forward and backward link are in the interior of a track life cycle. A track is *initiated* by one of the following situations: Either a new rain cell emerges, several cells merge, the track splits from a breaking cell, or it has no regular backward link because of missing values. Correspondingly, a track *terminates* either by dissolving, by splitting up, by merging with other cells, or it is interrupted by missing values. The states at the beginning and end of each track are recorded. The

advection field is derived on a  $5 \times 5$  grid of square grid boxes of  $180 \text{ km} \times 180 \text{ km}$  size (Figure 1f), coarse graining the full  $900 \text{ km} \times 900 \text{ km}$  study domain. This is performed by calculating the velocity vectors of the center of masses and determining their means and standard deviations within each coarse grid box and 6 h time interval. If less than five tracks are found within a coarse grid box or the standard deviation exceeds the mean, the velocity vector is regarded as unclear and marked as missing value. We choose a 6-hourly temporal resolution which matches the temporal resolution of wind fields provided by the ECMWF Re-Analysis (ERA)-Interim reanalysis data set [Dee et al., 2011] which we use for validation. Finally, the tracking is repeated in a *second iteration*, by using the additional information of the advection field (Figure 1g): Each cell identified in the first step is advected one time step into the future with the (spatially and temporally interpolated) velocity vector at its center of mass, before overlaps with cells of the successor time step are checked. The second iteration is able to find tracks which are not detected by the first iteration because some cells do not overlap with the consecutive time step. This is the

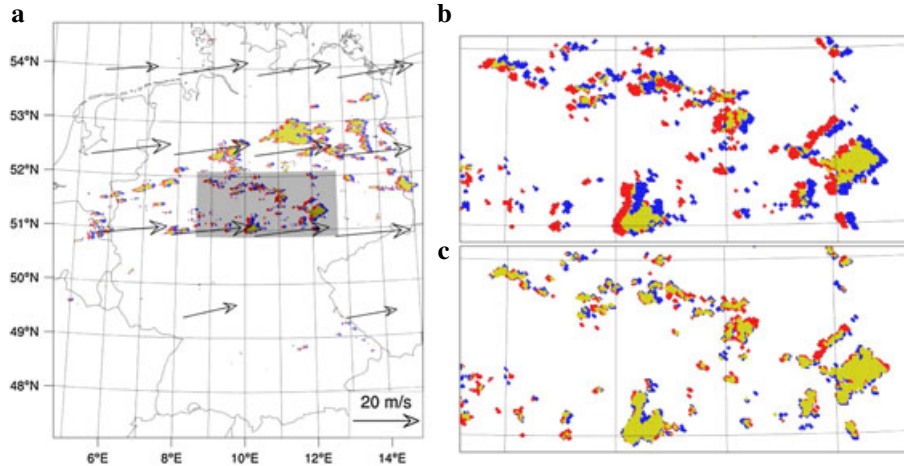


**Figure 2.** Iterative tracking procedure. (a) Rain cells during a specific predominantly convective situation on 10 May 2007, on a map showing the full domain of the radar data. Areas where the intensity exceeds the 0.6 mm h<sup>-1</sup> at 12:00 A.M. are shown in red; blue areas show the exceedance one time step later at 12:05 A.M. Overlapping areas, where the exceedance is found at both time steps are colored yellow. Arrows indicate the advection vector field in m s<sup>-1</sup>. (b) Zoom into the gray-shaded area in Figure 2a. (c) Similar as Figure 2b but all cells of the previous time step (red) are shifted 5 min into the future by the background flow. This results in a better overlap with the cells of the next time step (blue).

case if the cell diameter is smaller than its displacement by the advection field. Figure 2 shows an example situation for illustration. The iteration procedure is repeated until the tracking result converges to a stable state as measured by wind speed and correlations with reanalysis data.

### 3. Validation of the IRT Method

#### 3.1. Flow Velocities

[13] To demonstrate the convergence of the iteration process, we compare the background flow velocities of several iteration steps with ERA-Interim reanalysis wind vectors, using the threshold 0.6 mm h<sup>-1</sup>. As can be seen in Figure 3a, the mean flow speed increases with the number of iterations until approximately 12 m s<sup>-1</sup> after the fifth iteration, corresponding to a height level of approximately 800 hPa in the

ERA wind speed profile. The increase in flow speed with the number of iterations can be explained by the fact that at the earlier iterations, less fast-moving tracks are detected since small and fast cells do not overlap between time steps. In the consecutive iterations, more and more fast moving tracks are detected. The mean flow speed nearly converges at the sixth iteration, such that it is almost identical to the fifth one (only approximately 0.11 % difference). The correlation  $R(p)$  of the advection field  $\vec{v}_a$  with the ERA-Interim wind  $\vec{v}_e(p)$  at pressure levels  $p$  is shown in Figure 3b and is calculated as

$$R(p) = \frac{\langle (\vec{v}_a - \langle \vec{v}_a \rangle) \cdot (\vec{v}_e(p) - \langle \vec{v}_e(p) \rangle) \rangle}{\sqrt{\langle (\vec{v}_a - \langle \vec{v}_a \rangle)^2 \rangle \langle (\vec{v}_e(p) - \langle \vec{v}_e(p) \rangle)^2 \rangle}} \quad (1)$$

where  $\langle \dots \rangle$  denotes averaging over all defined grid boxes and time steps. For all iterations, the maximum correlation

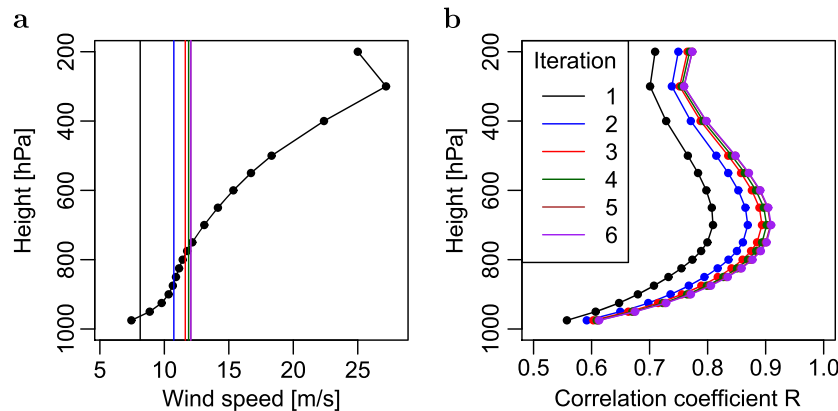


**Figure 3.** Validation of flow field detection. Comparison of flow velocities from six iterations (labeled “1”, ..., “6”) with ERA-Interim wind field (black points) on different pressure levels, averaged over the full data set. (a) Mean flow speeds (vertical lines) and vertical profile of ERA-Interim mean wind speed. (b) Correlation of flow vectors with ERA wind vectors.

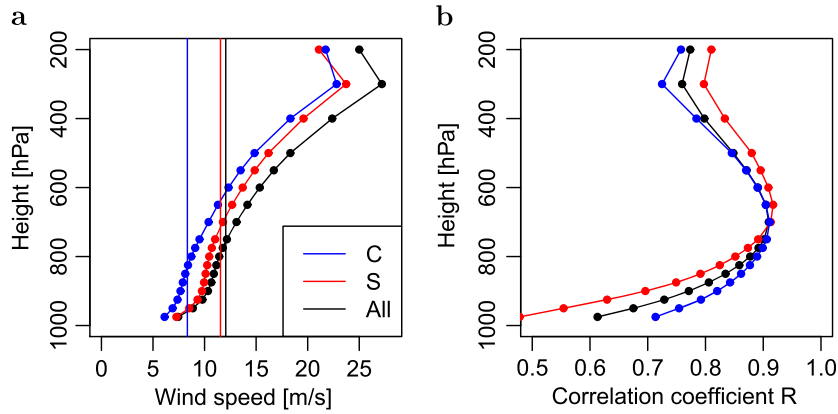


**Figure 4.** Flow field separated by precipitation type. Same as Figure 3 but separated for convective (C) and stratiform (S) type, for the sixth iteration and the  $Q_2$  classification criterion. Black lines refer to the mean over all data (All), i.e., including stratiform, convective, and mixed conditions.

is reached at the 700 hPa level, which is consistent with a typical height for precipitating clouds. Similar as for the flow speed, the correlation improves up to the fifth iteration and then saturates (approximately 0.13 % difference between the fifth and sixth iteration at 700 hPa).

[14] Figure 4 shows mean flow speed and correlation for the sixth iteration tracking result only but separately for situations classified as stratiform and convective, respectively, using the synoptic observations under the stricter  $Q_2$  criterion. The ERA-Interim wind speed profile (Figure 4a) shows lower values for convective situations, possibly due to weak large-scale forcing. Interestingly, even though wind speeds at stratiform conditions are higher, they are still lower than the total mean wind speed including also the mixed conditions. Therefore, it can be concluded that large wind speeds are usually associated with conditions which cannot be classified as strictly stratiform or convective. The flow speeds detected from the tracking show a similar behavior, with lowest speed for convective and higher speed for stratiform conditions. Again, the total mean is higher than both convective and stratiform, indicating that the highest wind speeds are found at mixed conditions. The intersection of the tracking flow speeds with the wind speed profiles also differs: It lies below 800 hPa for convective and approximately at the 700 hPa level for stratiform conditions. This is consistent with the correlation (Figure 4b), which reaches its maximum at a higher level for stratiform (approximately 650 hPa) than for convective (approximately 700 hPa) conditions.

### 3.2. Sensitivity Tests

[15] For sensitivity tests, we repeated the tracking with the higher threshold  $1.2 \text{ mm h}^{-1}$ , which corresponds to the typical measurement accuracy of rain gauges (0.1 mm per 5 min time interval). The total number of detected tracks with threshold  $0.6 \text{ mm h}^{-1}$  is almost 50% larger than with the latter (Figure 5a). This is not surprising: Precipitation intensity distributions are dominated by low intensity values. Therefore, much more rain cells are detected when the threshold is lower. However, if the threshold is too low, cells would grow too large with the side effect that distinct rain events would become connected. Also, noise would be more dominant in the detection procedure. After six iterations, a good convergence of the cell number can be seen for the

threshold  $0.6 \text{ mm h}^{-1}$ . In contrast, for  $1.2 \text{ mm h}^{-1}$  the convergence is much less homogeneous, and six iterations do not seem to be sufficient. This behavior is also seen for the correlation with the ERA-Interim wind field at 700 hPa (Figure 5b): It is higher for the  $0.6 \text{ mm h}^{-1}$  threshold and converges clearly faster. Only the convergence of the mean flow speed is very similar in both cases (Figure 5c).

[16] Additionally, we tested the sensitivity of the tracking method to reduced spatial and temporal resolution. In the first case, we lowered the horizontal resolution of the radar data from 1 km to 2 km, by averaging intensity over boxes of  $2 \times 2$  pixels. In the second test, we increased the time interval from 5 to 10 min by omitting every second radar image. Two

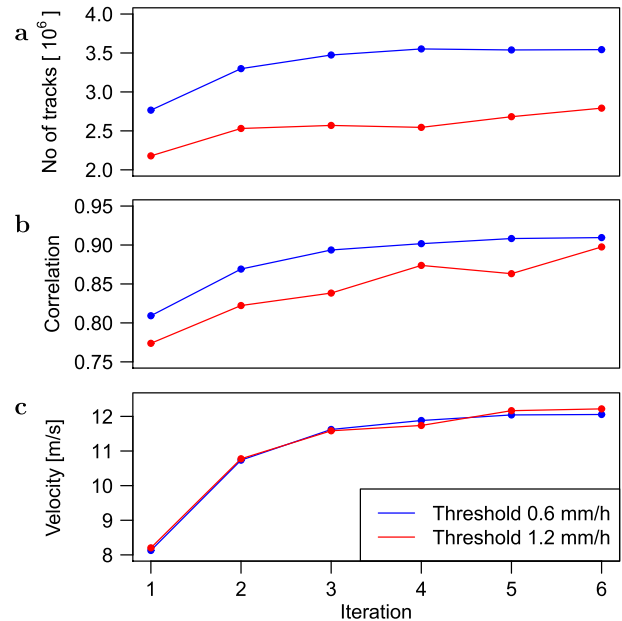


**Figure 5.** Convergence of the iteration process. (a) Total number of detected tracks, (b) correlation coefficient of flow field with ERA-Interim wind at the 700 hPa level, and (c) advection velocity, plotted against the number of iterations 1–6. Blue (red) curves show iterations with intensity threshold 0.6 (1.2)  $\text{mm h}^{-1}$ .

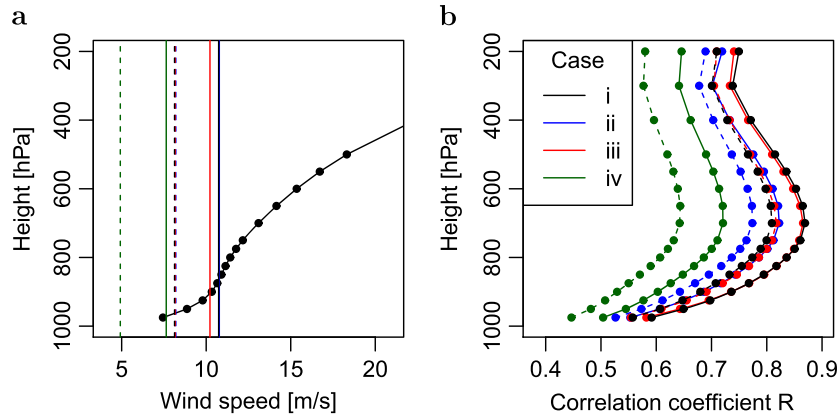


**Figure 6.** Sensitivity tests. Same as Figure 3 but for different thresholds, horizontal, and temporal resolutions. First (dashed lines) and second (solid lines) iterations only. (i) Threshold  $0.6 \text{ mm h}^{-1}$ , 1 km horizontal resolution, 5 min temporal resolution; (ii)  $1.2 \text{ mm h}^{-1}$ , 1 km, 5 min; (iii)  $0.6 \text{ mm h}^{-1}$ , 2 km, 5 min; (iv)  $0.6 \text{ mm h}^{-1}$ , 1 km, 10 min. In panel (a), the dashed black, red, and blue lines lie on top of each other. The same is the case for the solid black and blue lines.

iterations were performed for each test, using the threshold. The resulting flow speed and correlation is shown in Figure 6, together with the full-resolution tracking result with the threshold  $1.2 \text{ mm h}^{-1}$ . The highest correlation with ERA-interim wind is reached with full spatial and temporal resolution of the data set and the threshold  $0.6 \text{ mm h}^{-1}$ . However, the tracking result with 2 km spatial resolution reaches a comparable level of correlation, and an only slightly lower mean wind speed. In contrast, the full-resolution result with the higher threshold  $1.2 \text{ mm h}^{-1}$  reaches the same mean wind speed, but a lower correlation. To take full advantage of the data, we decided to use the full resolution of the data for the life cycle statistics, using the faster convergent threshold  $0.6 \text{ mm h}^{-1}$ .

[17] A clearly worse result is found with the 10 min temporal resolution: Both mean flow speed and correlation of the second iteration are still lower than the first iteration result with the 5 min interval and the same threshold. Especially for smaller cells, a 10 min time interval seems to be too large to establish links between time steps for a successful tracking.

## 4. Track Life Cycles

### 4.1. Track Detection and Mean Profiles

[18] Given the above discussion on convergence, we use the tracking result of the sixth iteration, consisting of  $3.54 \times 10^6$  detected tracks, to study track profiles. To obtain a clear picture of the temporal behavior of rain cells from their onset to their dissolution, we choose only the subset of tracks which do not split or merge, and thus have a unique life cycle. This means that all tracks which begin or terminate by merging or splitting are removed from the statistics and thus have no effect on the results. Further, all tracks which are contaminated by missing values are removed. Approximately 27% of all detected tracks satisfy this condition, leaving the sample size large enough for a proper analysis.

[19] The distribution functions of these tracks as function of duration (Figure 7) show an approximate power law distribution, especially for the stratiform tracks. We distinguish

the two classification criteria  $Q1$  and  $Q2$ . The stricter criterion  $Q2$  diminishes the sample size by nearly an order of magnitude in the case of stratiform tracks but considerably less in the case of convective tracks. In fact, for the  $Q1$  criterion, there are more stratiform ( $2.1 \times 10^5$ ) than convective tracks ( $1.3 \times 10^5$ ), while for  $Q2$  the opposite is true ( $3.8 \times 10^4$  versus  $5.6 \times 10^4$ , respectively). The stratiform classification is more sensitive to contamination by embedded convection in the systems. In the following, we will make frequent use of these two criteria. Note that the analysis is constrained to tracks with durations up to 60 min as the sample sizes decrease strongly beyond this point.

### 4.2. Temporal Evolution

[20] In Figure 8 we show the average temporal development of the mean track intensity for tracks classified according to their duration. Each line in the panels corresponds to the average taken over all tracks of a given duration and the conditions specified in the plot and caption. To test for sensitivity on the strictness criteria, we compare the  $Q2$  criterion (Figures 8a and 8e) to the  $Q1$  criterion

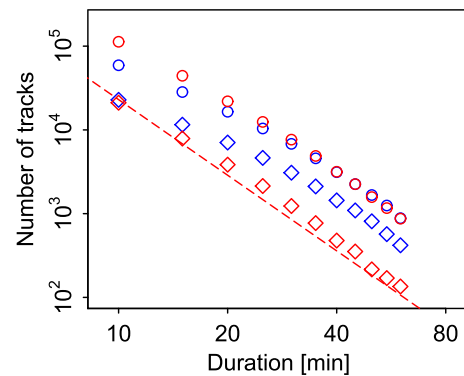


**Figure 7.** Distribution of track durations. Red (blue) curves show the distribution of all recorded stratiform (convective) tracks using the  $Q1$  criterion (circles) and the  $Q2$  criterion (diamonds). The dashed line represents a power law of exponent  $-3$ . Note on the double logarithmic axes.



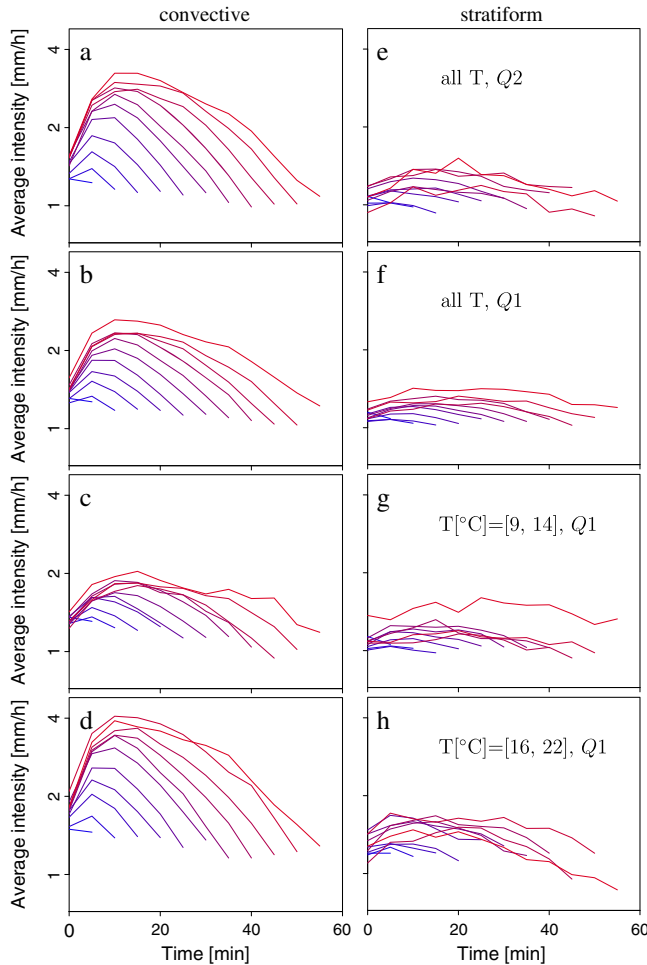


**Figure 8.** Intensity profiles of tracks. Intensity profiles of tracks averaged over all realizations of tracks of a given length. Colors from dark blue to bright red indicate tracks of durations from 5 to 60 min, respectively. (a) Convective tracks for all temperatures for  $Q2$  criterion. (b) Same as Figure 8a but for  $Q1$  criterion. (c) Same as Figure 8a but for  $T[^\circ\text{C}] = [9, 14]$ . (d) Same as Figure 8a but for  $T[^\circ\text{C}] = [16, 22]$ . (e–h) Corresponding results for stratiform tracks.  $T$  is the E-OBS daily mean temperature. Note on the logarithmic vertical axes.

(Figures 8b and 8f). The stricter  $Q2$  criterion leads to somewhat more pronounced peaks for convective precipitation, but the qualitative behavior is very similar. Note also that the curves for the stratiform type are more jumpy in the case of the  $Q2$  criterion, attributable to the smaller amount of data for the stricter criterion especially for this type (compare Figure 7). We therefore proceed by using the  $Q1$  criterion for conditional probabilities as this criterion allows for a larger sample size. Generally, it is found that longer tracks have generally larger average intensities for both convective (Figures 8a and 8b) and stratiform (Figures 8e and 8f) tracks. To understand this behavior, we note that precipitation is correlated over time [Berg *et al.*, 2013]. Weak tracks are more likely to be cut by the threshold used to define onset and dissipation of the track, and are thereby viewed as shorter tracks. However, in addition, intensities increase much more strongly for convective tracks than for stratiform

tracks. Even more strikingly, convective tracks show a characteristic temporal profile: During the first third of the track, intensities steeply increase and produce a well-defined peak. The tracks then decay relatively steadily. This behavior is visible for both the low (Figure 8c) and high (Figure 8d) temperature ranges, with the only difference that the peak intensity increases more strongly for higher temperature. We interpret these findings as the manifestation of a *track life cycle* in the case of convective tracks, which is invigorated with increasing temperature.

[21] Stratiform tracks show no clear structure as a function of time. Only at high temperatures (Figure 8h) there is some visible structure. However, at these temperatures, a mixing of types with convective activity could also be a possible cause of distortion, as noted above. Overall, the curves for different track durations are rather horizontal, there is no clear evidence of a *life cycle*. Here, generally similar features are obtained, however with an even more pronounced invigoration for the convective tracks.

[22] In Figure 9 we present a summary of results for the peak timing and the corresponding intensities. For convection (Figure 9a), peak intensities increase strongly with temperature and are almost twice as high for the higher temperature range. There is furthermore a tendency for the peak to occur closer to the beginning of the tracks. For stratiform tracks (Figure 9b), the timing of the peak is less clear, with large differences for the different durations, but with a general tendency to occur slightly shifted to the first half of the track. The weak increase of peak intensities with temperature seems to occur right after the first third of the track, indicating again that this might be due to sample contamination from embedded convection. For stratiform tracks, random scattering of data appears to be the most plausible interpretation. No such asymmetry is visible in the mean profiles of the cell area, which peaks at intermediate times (plots not shown). Longer tracks generally produce larger cell areas.

#### 4.3. Extreme Tracks

[23] We now consider extremes as measured by tracks with average intensity (as taken over their total duration) above the 90th percentile of all tracks for each duration. Figures 10a, 10b, 10e, and 10f show that there are no substantial differences between the two criteria  $Q1$  and  $Q2$  except for less noise and slightly weaker intensities for  $Q1$ . We therefore again use the  $Q1$  criterion—where more data are available—for the analysis of the different temperature ranges.

[24] Overall, the extreme tracks behave similar to the average track profiles, i.e., with no clear structure for stratiform tracks, whereas convective tracks show a clear life cycle with peak near 1/3 of the track, increasing intensities with duration and a strong temperature dependency. However, the steep increase of intensities at the onset of the tracks is even more clear than for the analysis of the average profiles.

[25] When performing a direct comparison of the two types (Figures 10b and 10f) it becomes apparent that the life cycle of convective tracks yields extended periods (especially near approximately 1/3 of the track duration) where these tracks produce significantly heavier precipitation than their stratiform counterpart, especially at higher

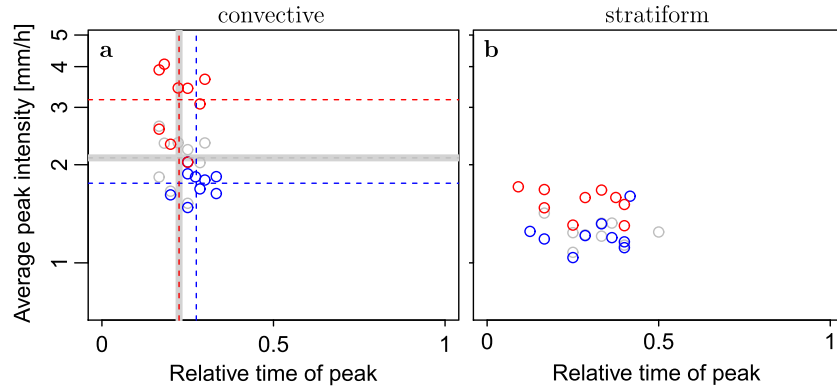


**Figure 9.** Peak timing and intensity. Average timing of peak intensity relative to the normalized lifetime of tracks, plotted against the corresponding peak intensities, conditional of precipitation type, and temperature. Red points correspond to mean values of tracks with durations of 20, 25, . . . , 60 min, respectively, in the temperature range  $T/^{\circ}\text{C} = [16, 22]$ ; blue points are respectively for  $T/^{\circ}\text{C} = [9, 14]$ . Gray points are data without distinction of temperature. Correspondingly, colored dashed lines and thick gray lines indicate means. (a) Convective and (b) stratiform results, respectively. Note on the logarithmic vertical axis.

temperatures (Figures 10d and 10h). This feature is important for risk assessment for local flooding: When the track passes over a stationary observer, the prevailing flow of the atmosphere will typically translate the track across the observer within less than 30 min [Berg *et al.*, 2013], i.e., the perceived duration of a track to an observer on the ground. During this duration, a convective track will then have the potential to produce much heavier rains than does a stratiform track. Near the onset and decay of the track, convective tracks often show lower intensities than stratiform tracks. However, the mean intensities taken over the entire track duration (crossed symbols) are only marginally higher for convective than for stratiform tracks. An interesting observation is that in the case of convection, those temporal means increase with duration for high temperatures, while a decrease is visible for lower temperatures. No such observation can be made for the stratiform type. This observation could again be seen as a reflection of the stronger temporal correlation present in the convective cell life cycle [Berg *et al.*, 2013]: Tracks that produce stronger extremes are overall more powerful. The simple analysis shown in Figure 10 makes clear that the existence of a life cycle per se can imply a potential for more pronounced extreme tracks.

#### 4.4. Temperature Response of Extremes

[26] The temperature response of precipitation extremes has been discussed recently in the literature [Lenderink and van Meijgaard, 2008]. Exceedance of the Clausius-Clapeyron rate was observed for temperature ranges between approximately 12 and 22°C, and it was later suggested that this increase could be attributable mainly to convective type precipitation for instantaneous and event-mean precipitation intensities [Berg *et al.*, 2013]. In Figure 11 we perform an analogous analysis, but explicitly resolving the track life cycle. We first extract the data corresponding to the percentile range [0.7, 0.975] and a given track duration for the two temperature ranges [9, 14]°C and [16, 22]°C. To test, in how far intensity increases with temperature are described by the Clausius-Clapeyron relation—an approximately exponential increase of the form  $I(T) \propto \exp(\alpha T)$ —

we produce intensity ratios  $I(T_2)/I(T_1) \propto \exp(\alpha(T_2 - T_1)) \equiv r$ , with  $r$  being the ratio of two corresponding intensity percentiles (i.e., matching track duration and time step). Here,  $T_1$  and  $T_2$  are taken as the means of all track temperatures within the temperature ranges [9, 14]°C and [16, 22]°C, respectively. Similarly,  $I(T_2)$  and  $I(T_1)$  are the corresponding mean intensities, taken at a certain time step within the track life cycle. To allow sufficient amounts of data, we require at least 200 tracks for each category. All other tracks are left out of the analysis. To obtain the coefficient  $\alpha$  of temperature increase, we hence use  $\alpha = \log(r)/(T_2 - T_1)$ . Collecting all resulting ratios for different track durations and several percentiles, to minimize noise, we rescale all tracks of different durations to length unity. Thereby, we are then able to average over all track durations. The results (Figure 11) show that  $\alpha$  in the case of heavy convective precipitation indeed exceeds the Clausius-Clapeyron rate of 7% for most of the track duration. Our data show that during the first third of the track duration, a general peak of exceedance is observed. We however point out that detection of this peak is somewhat obscured by the presence of noise and should be verified using a larger data set. In comparison, using the  $Q1$  criterion, stratiform tracks show only a slight exceedance of the Clausius-Clapeyron rate and no obvious structure as a function of the relative track duration. The exceedance of the Clausius-Clapeyron rate there may again be an artifact of contamination by convective data in the stratiform category and almost vanishes if the  $Q2$  criterion is applied.

## 5. Discussion and Conclusion

[27] We have proposed a new iterative rain cell tracking method (IRT). By sensitivity analysis and comparison to reanalysis wind fields, IRT has been shown to be suitable for obtaining a Lagrangian view in which the dominant flow field is taken into account in order to follow precipitation events throughout their life cycles. The new features of IRT are the iterative improvement of cell detection and the fact that it determines the large-scale background flow while preserving the relative small-scale dynamics—these



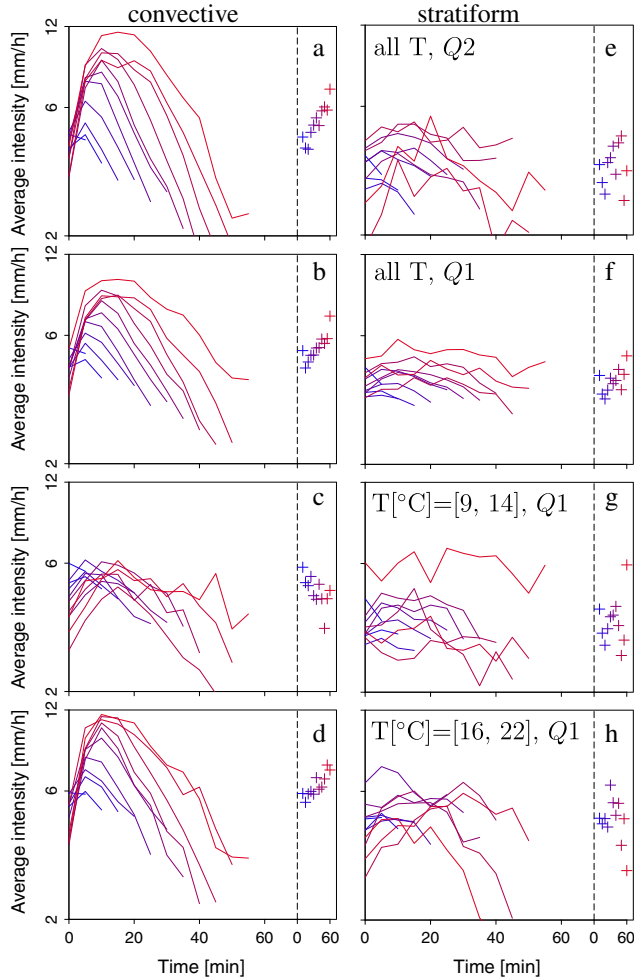


**Figure 10.** Comparison of extremes. Average precipitation intensity as function of time after track initiation for all (a–d) convective and (e–h) stratiform tracks above the 90th percentile of mean track intensities in the respective categories. Figure 10a denotes  $Q2$  criterion for all observed temperatures. Figure 10b shows  $Q1$  criterion for all observed temperatures. Figure 10c depicts  $Q1$  criterion for low temperatures  $T/^{\circ}\text{C} = [9, 14]$ . Figure 10d shows  $Q1$  criterion for high temperatures  $T/^{\circ}\text{C} = [16, 22]$ . Similar criteria apply for Figures 10e–10h for the stratiform tracks. The less strict  $Q1$  criterion is shown because there is relatively limited data once the 90th percentile is extracted and further conditions (temperature and type) are applied. Colored crosses indicate temporal means taken over the track durations with corresponding colors. Note on the logarithmic vertical axis.

may be produced by the cloud and could be used for further analysis of intercloud dynamics [Koren and Feingold, 2011; Feingold et al., 2010]. In the present article, however, we make use of the tracks and the large-scale flow. The repeated iteration process of the tracking yields a good correlation with the wind field from ERA-Interim reanalysis data after six iterations, especially at a height level of approximately 700 hPa. We have shown that a reduction of the horizontal resolution from 1 km to 2 km does not affect the quality of tracking results. On the other hand, a high temporal radar image frequency of 5 min is necessary for a

reasonable tracking of convective cells. This should be kept in mind for modeling studies at convection permitting or convection resolving scales, when the model output interval has to be chosen adequately.

[28] Synoptic cloud observations allow a separation between stratiform and convective track types and reveal a clearly different behavior of their life cycles. Stratiform tracks do not show characteristic life cycles, and therefore, it might be invalid to speak of them as distinct entities. Instead, they may be better described as randomly formed contiguous structures embedded into the bulk of a larger-scale precipitating field. On the other hand, convective cells show a characteristic temporal behavior, indicating that they are units which must be regarded as separate from their surrounding but which however are in close contact to their environment and compete for and exchange moisture and energy. While our study cannot give direct insight into the dynamical and thermodynamical 3-D structure of convective storms, it shows their impact on surface precipitation and the sensitivity to surface air temperatures. For all track durations, peak intensities strongly increase with temperature, reflecting the super-CC increase found for convective rain intensities. A striking feature is the time asymmetry of the mean intensity profiles, with a shift of the peak intensity toward the beginning of the tracks. This shift is stronger for higher temperatures. Note that the average time development may somewhat deviate if merging cells were included into the analysis. These were deliberately excluded in the present

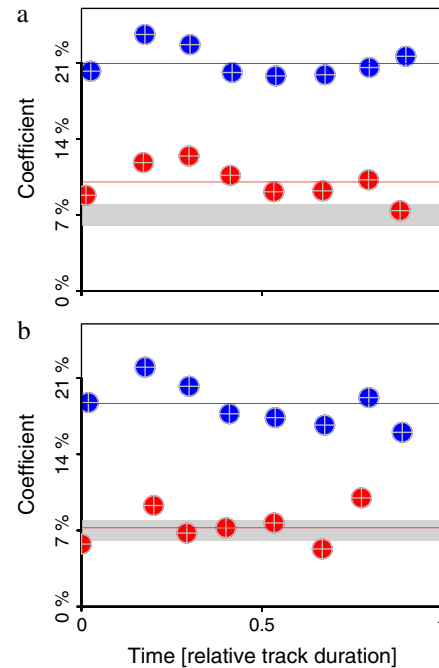


**Figure 11.** Change of heavy precipitation with temperature. (a) Large symbols denote averages for the coefficient  $\alpha$ , which is a measure for the temperature response of the precipitation intensity. The relative time development of  $\alpha$  over a normalized track duration is shown for convective (blue) and stratiform (red) precipitation intensity for the  $Q1$  criterion. The gray thick line marks the 7% CC increase. (b) Similar to Figure 11a but for the  $Q2$  criterion.

study. To include them, the IRT method has to be extended to handle merging cells.

[29] The steep increase in intensity at the beginning of the track is even more obvious when extreme tracks are considered. A comparison with the corresponding extreme stratiform tracks shows a similar temporal mean. However, there seems to be a typical time period of approximately 30 min, beginning shortly after the track initialization, in which extreme convective event intensities strongly exceed the mean. In contrast, average stratiform event intensities fluctuate only weakly around their mean. This observation raises important concerns regarding risk assessment of catastrophic, local downpours, such as flash floods.

[30] The analysis of the ratio between intensities at low and high temperatures show a strong exceedance of the Clausius-Clapeyron rate for convective precipitation. The data suggest the presence of a peaked exceedance at the onset of convective tracks, which could be indicative of the strong dynamics leading to the super-Clausius-Clapeyron behavior for higher temperatures, where invigorated moist convection at the onset of the event can saturate the cloud to a higher degree. However, we cannot provide robust evidence for the existence of this peak within this study.

[31] Investigations of the 3-D behavior of the convective events are essential for a deeper understanding of the changes in dynamics at increasing temperature. Such analysis can be performed with volumetric radar data and also by using large eddy simulations [Bretherton *et al.*, 2005; Tompkins and Craig, 1998] and convection resolving regional climate model simulations. We propose in-depth studies using such tools to further explore the physical processes leading to the invigoration of convection with increasing temperature.

[32] **Acknowledgments.** The authors acknowledge the radar data from the German Weather Service (DWD), synoptic codes from the Met Office Integrated Data Archive System, retrieved through the British Atmospheric Data Centre (BADC), and the E-OBS data set from the EU-FP6 project ENSEMBLES (<http://ensembles-eu.metoffice.com>) and the data providers in the ECA&D project (<http://eca.knmi.nl>). C.M. acknowledges support from Max Planck Institute for Meteorology through the project KLIFF, funded by the Ministry of Science and Education of Lower Saxony, Germany, and from Helmholtz-Zentrum Geesthacht. P.B. acknowledges support from SMHI, and J.O.H. acknowledges support by the Danish National Research Foundation through the Center for Models of Life.

## References

- Berg, P., C. Moseley, and J. O. Haerter (2013), Strong increase in convective precipitation in response to higher temperatures, *Nat. Geosci.*, **6**, 181–185.
- Bretherton, C. S., P. N. Blossey, and M. Khairoutdinov (2005), An energy-balance analysis of deep convective self-aggregation above uniform SST, *J. Atmos. Sci.*, **62**, 4273–4292.
- Chen, G., H. Xue, W. Zhang, and X. Zhou (2012), The three-dimensional structure of precipitating shallow cumuli. Part one: The kinematics, *Atmos. Res.*, **112**, 70–78.
- Crewell, S., et al. (2008), The general observation period 2007 within the priority program on quantitative precipitation forecasting: Concept and first results, *Meteorol. Z.*, **17**, 849–866.
- Dee, D. P., et al. (2011), The ERA-Interim reanalysis: Configuration and performance of the data assimilation system, *Q. J. R. Meteorol. Soc.*, **137**, 553–597.
- Dixon, M., and G. Wiener (1993), Titan: Thunderstorm identification, tracking, analysis, and nowcasting—A radar-based methodology, *J. Atmos. Oceanic Technol.*, **10**, 785–797.
- Feingold, G., I. Koren, H. Wang, H. Xue, and W. A. Brewer (2010), Precipitation-generated oscillations in open cellular cloud fields, *Nature*, **466**, 849–852.
- Feng, Z., X. Dong, B. Xi, S. A. McFarlane, A. Kennedy, B. Lin, and P. Minnis (2012), Life cycle of midlatitude deep convective systems in a Lagrangian framework, *J. Geophys. Res.*, **117**, D23201, doi:10.1029/2012JD018362.
- Handwerker, J. (2002), Cell tracking with TRACE3D—A new algorithm, *Atmos. Res.*, **61**, 15–34.
- Haylock, M. R., N. Hofstra, A. M. G. Klein Tank, E. J. Klok, P. D. Jones, and M. New (2008), A European daily high-resolution gridded data set of surface temperature and precipitation for 1950–2006, *J. Geophys. Res.*, **113**, D20119, doi:10.1029/2008JD010201.
- Hering, A., S. Senesi, P. Ambrosetti, and I. Bernard-Bouissieres (2005), Nowcasting thunderstorms in complex cases using radar data, *WWRP Symposium on Nowcasting and Very Short Range Forecasting, September 5th–9th 2005, Toulouse*, 2.14.
- Houze Jr., R. A. (1997), Stratiform precipitation in regions of convection: A meteorological paradox?, *Bull. Am. Meteorol. Soc.*, **78**, 2179–2226.
- Johnson, J., P. MacKeen, A. Witt, M. DeWayne, G. Stumpf, M. Eilts, and K. Thomas (1998), The storm cell identification and tracking algorithm: An enhanced WSR-88D algorithm, *Weather Forecasting*, **13**, 263–276.
- Koren, I., and G. Feingold (2011), Aerosol-cloud-precipitation system as a predator-prey problem, *Proc. Natl. Acad. Sci. U.S.A.*, **108**, 12,227–12,232.
- Kysnarova, H., and P. Novak (2009), CELLTRACK—Convective cell tracking algorithm and its use for deriving life cycle characteristics, *Atmos. Res.*, **93**, 317–327.
- Lakshmanan, V., K. Hondl, and R. Rabin (2009), An efficient, general-purpose technique for identifying storm cells in geospatial images, *J. Atmos. Oceanic Technol.*, **26**, 523–537.
- Lenderink, G., and E. van Meijgaard (2008), Increase in hourly precipitation extremes beyond expectations from temperature changes, *Nat. Geosci.*, **1**, 511–514.
- Llasat, M.-C. (2001), An objective classification of rainfall events on the basis of their convective features: Application to rainfall intensity in the northeast of Spain, *Int. J. Climatol.*, **21**, 1385–1400.
- Novo, S., D. Martinez, and O. Puentes (2013), Tracking, analysis, and nowcasting of Cuban convective cells as seen by radar, *Meteorol. Appl.*, doi:10.1002/met.1380.
- Peleg, N., and E. Morin (2012), Convective rain cells: Radar-derived spatiotemporal characteristics and synoptic patterns over the eastern Mediterranean, *J. Geophys. Res.*, **117**, D15116, doi:10.1029/2011JD017353.
- Rigo, T., N. Pineda, and J. Bech (2012), Analysis of warm season thunderstorms using an object-oriented tracking method based on radar and total lightning data, *Nat. Hazards Earth Syst. Sci.*, **10**, 1881–1893.
- Rosenfeld, D. (1987), Objective method for analysis and tracking of convective cells as seen by radar, *J. Atmos. Oceanic Technol.*, **4**, 422–434.
- Singleton, A., and R. Toumi (2012), Super-Clausius-Clapeyron scaling of rainfall in a model squall line, *Q. J. R. Meteorol. Soc.*, **139**, 334–339.
- Smyth, T., and A. Illingworth (1998), Radar estimates of rainfall rates at the ground in bright band and non-bright band events, *Q. J. R. Meteorol. Soc.*, **124**, 2417–2434.
- Steiner, M., R. A. Houze Jr., and S. E. Yuter (1995), Climatological characterization of three-dimensional storm structure from operational radar and rain gauge data, *J. Appl. Meteorol.*, **34**, 1978–2007.
- Steiner, M., J. A. Smith, and R. Uijlenhoet (2004), A microphysical interpretation of radar reflectivity-rain rate relationships, *J. Atmos. Sci.*, **61**, 1114–1131.
- Taylor, G. (1938), The spectrum of turbulence, *Proc. R. Soc. London, Ser. A*, **164**, 476–490.
- Tompkins, A. M., and G. C. Craig (1998), Radiative-convective equilibrium in a three-dimensional cloud-ensemble model, *Q. J. R. Meteorol. Soc.*, **124**, 2073–2097.
- Wilson, J., N. Crook, C. Mueller, J. Sun, and M. Dixon (1998), Nowcasting thunderstorms: A status report, *Bull. Am. Meteorol. Soc.*, **79**, 2079–2099.